

# Interferometry and coherent single-electron transport through hybrid superconductor-semiconductor Coulomb islands

A. M. Whiticar,<sup>1,\*</sup> A. Fornieri,<sup>1,\*</sup> E. C. T. O’Farrell,<sup>1</sup> A. C. C. Drachmann,<sup>1</sup> T. Wang,<sup>2,3</sup> C. Thomas,<sup>2,3</sup> S. Gronin,<sup>2,3</sup> R. Kallaheer,<sup>2,3</sup> G. C. Gardner,<sup>2,3</sup> M. J. Manfra,<sup>2,3,4,5</sup> C. M. Marcus,<sup>1,†</sup> and F. Nichele<sup>1,‡</sup>

<sup>1</sup>*Center for Quantum Devices, Niels Bohr Institute,  
University of Copenhagen and Microsoft Quantum Lab Copenhagen,  
Universitetsparken 5, 2100 Copenhagen, Denmark*

<sup>2</sup>*Department of Physics and Astronomy and Microsoft Quantum Lab Purdue,  
Purdue University, West Lafayette, Indiana 47907 USA*

<sup>3</sup>*Birck Nanotechnology Center, Purdue University, West Lafayette, Indiana 47907 USA*

<sup>4</sup>*School of Materials Engineering, Purdue University, West Lafayette, Indiana 47907 USA*

<sup>5</sup>*School of Electrical and Computer Engineering,  
Purdue University, West Lafayette, Indiana 47907 USA*

(Dated: December 14, 2021)

Majorana zero modes are leading candidates for topological quantum computation due to their non-local character and non-abelian exchange statistics [1, 2]. Among their attributes, spatially separated Majorana modes are expected to allow coherent single-electron transport through one-dimensional topological superconductors in the Coulomb blockade (CB) regime [3]. We have investigated this feature by patterning an elongated epitaxial InAs-Al Coulomb island embedded in an Aharonov-Bohm interferometer. Using a parallel magnetic field to lower the energy of a discrete sub-gap state in the island below its charging energy, conductance oscillations in the ring were observed with a flux period of  $h/e$  ( $h$  is Planck’s constant and  $e$  is the elementary charge), indicating coherent single-electron transport through the interferometer. Oscillation amplitude was largest when CB conductance peaks in the island were  $1e$  periodic, and suppressed when CB was  $2e$  periodic or when superconductivity was suppressed. Oscillation phase shifts of  $\pi$  were observed when the charge occupancy of the island was changed by  $1e$ , indicating that the interferometer can detect island parity. Magnetic fields oriented orthogonal to the island reduced the field at which  $2e$  periodic peaks split and where coherent transport could also be observed, suggesting additional non-Majorana mechanisms for  $1e$  transport through these moderately short wires.

Initial experiments reporting signatures of Majorana zero modes (MZMs) in hybrid superconductor-semiconductor nanowires focussed on zero-bias conductance peaks (ZBPs) using local tunnelling spectroscopy [4–7]. Subsequently, Majorana islands in the Coulomb blockade (CB) regime provided additional evidence of MZMs based on nearly  $1e$ -spaced CB peaks [8], and indicated a Rashba-like spin orbit coupling (SOC)

with spin-orbit field lying in-plane, perpendicular to the wire axis [9]. Under some circumstances, these signatures can be mimicked by trivial modes [10, 11], motivating a new generation of experiments that explicitly probe non-local properties, which are more difficult to mimick. For instance, non-locality of MZMs was recently investigated by measuring the energy splitting induced by the interaction of a quantum dot and a zero-energy state in a hybrid nanowire [12].

Non-locality can also be accessed by interferometric measurements of a Majorana island, where CB couples separated MZMs and fixes fermion parity [3, 13–16]. Single electrons tunnelling through a Majorana island are expected to be coherently transferred between MZMs via a process referred to as electron teleportation [3]. Coherent single-electron tunnelling through a CB island is a signature of non-locality, though not necessarily of MZMs, which require other signatures as well, as discussed in detail below. For example, the predicted absence of phase lapses through a CB peak in the transmission through the interferometer is a specific signature of MZMs [16]. To probe the non-locality of Majorana modes, a Majorana island can be embedded in the arm of an Aharonov-Bohm (AB) interferometer. If single-electron transport in both the reference arm and the Majorana island is coherent, conductance through the interferometer is expected to show magnetic flux modulations with period  $h/e$  [17]. The same approach was used to investigate coherent transport in semiconductor quantum dots [18–21].

Devices were fabricated using an InAs two-dimensional electron gas (2DEG) heterostructure covered by 8 nm of epitaxially grown Al [22]. The bare 2DEG (without Al) showed a phase coherence length of  $l_\phi \sim 4 \mu\text{m}$  (see Supplementary Fig. S.1). Figure 1a shows a micrograph of device 1 with a  $1.2 \mu\text{m}$  long and  $0.1 \mu\text{m}$  wide superconducting Al stripe formed by wet etching. Ti/Au top-gates were evaporated on top of a 25 nm  $\text{HfO}_2$  dielectric grown by atomic layer deposition. We studied two lithographically similar interferometers with circumferences

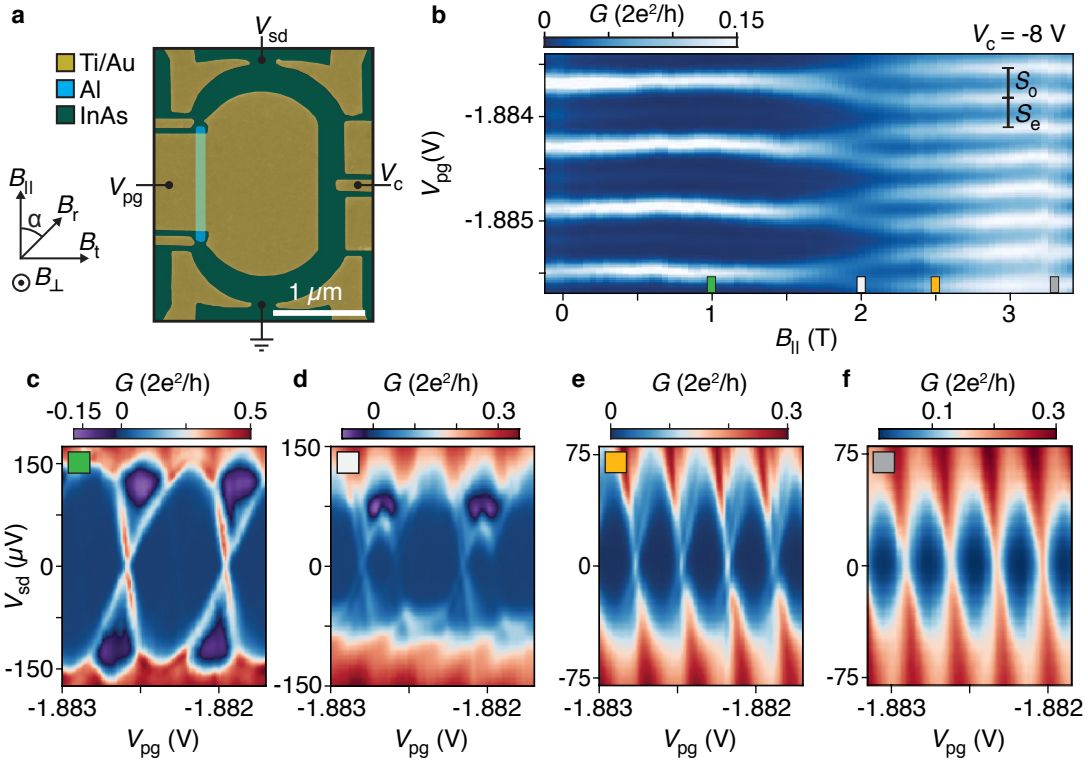


**FIG. 1. Hybrid Coulomb island interferometer.** **a**, False-colour electron micrograph of the Coulomb island interferometer where an Al wire (light blue) is embedded in a normal conducting Aharonov-Bohm interferometer (green) defined by Ti/Au gates (yellow). The gate voltage  $V_{pg}$  defines both the Coulomb island and the interferometer center, and controls the electron occupancy. The gate voltage  $V_c$  controls the resistance of the reference arm and  $V_{sd}$  is the source-drain dc bias voltage. Magnetic field directions are shown with  $\alpha$  denoting the in-plane angle measured with respect to the wire direction. **b**, Zero-bias differential conductance  $G$  as a function of  $B_{\parallel}$  and  $V_{pg}$ . **c-f**, Differential conductance  $G$  as a function of  $V_{sd}$  and  $V_{pg}$  showing Coulomb diamonds for  $B_{\parallel} = 1$  T (c), 2 T (d), 2.5 T (e), and 3.3 T (f). The measurements shown in panels b-f were taken with the reference arm closed.

of  $5.6 \mu\text{m}$  for device 1 and  $5 \mu\text{m}$  for device 2.

Applying a negative voltage,  $V_{pg}$ , to the central gate serves two purposes. It depletes the 2DEG surrounding the Al wire to form both the Coulomb island and the AB ring center and also adjusts the chemical potential and charge occupancy of the island. Energizing all exterior gates confines the 2DEG into an AB interferometer by connecting the Coulomb island to a normal conducting reference arm. The resistance of the reference arm was independently tuned by a negative gate voltage  $V_c$ . A source-drain bias voltage ( $V_{sd}$ ) was applied to one lead and the resulting current and four-terminal voltage was recorded. The in-plane magnetic fields  $B_{\parallel}$  and  $B_t$ , and perpendicular field,  $B_{\perp}$ , were controlled by a three-axis vector magnet.

At low temperatures, tunneling of single electrons onto an island with a superconducting gap  $\Delta$  is suppressed by CB, except at charge degeneracies. When the lowest sub-gap state energy,  $E_0$ , exceeds the charging energy  $E_c$ , ground-state degeneracies only occur between even-occupied states, resulting in  $2e$ -periodic CB conductance peaks [23]. Odd-occupied ground states are lowered into

the accessible spectrum by a Zeeman field, resulting in even-odd CB peak spacing when  $0 < E_0 < E_c$ . The difference in peak spacings between even and odd states,  $S = S_e - S_o$ , is proportional to  $E_0$  [8]. For well-separated MZMs,  $E_0$  tends exponentially toward zero, yielding  $1e$  periodic Coulomb peaks [24]. When the MZMs are not widely separated, CB peak spacings oscillate with field and density [8–10].

We first investigated the Coulomb island without interferometry by depleting a segment of the reference arm with gate voltage  $V_c$  (see Fig. 1a). Figure 1b shows zero-bias differential conductance  $G = dI/dV$  of the island as a function of parallel magnetic field  $B_{\parallel}$  and gate voltage  $V_{pg}$ , which controls the electron occupancy of the island. CB peaks are  $2e$  periodic at zero field and split around 2 T, becoming  $1e$  periodic as the sub-gap state moves toward zero energy. Measuring  $G$  as a function of both source-drain bias  $V_{sd}$  and  $V_{pg}$  reveals Coulomb diamonds (Fig. 1c-f). At low  $B_{\parallel}$ , diamonds are  $2e$  periodic with distinct negative differential conductance (Fig. 1c), which transition to an even-odd peak spacing difference at moderate fields (Fig. 1d), similar to previous work on super-

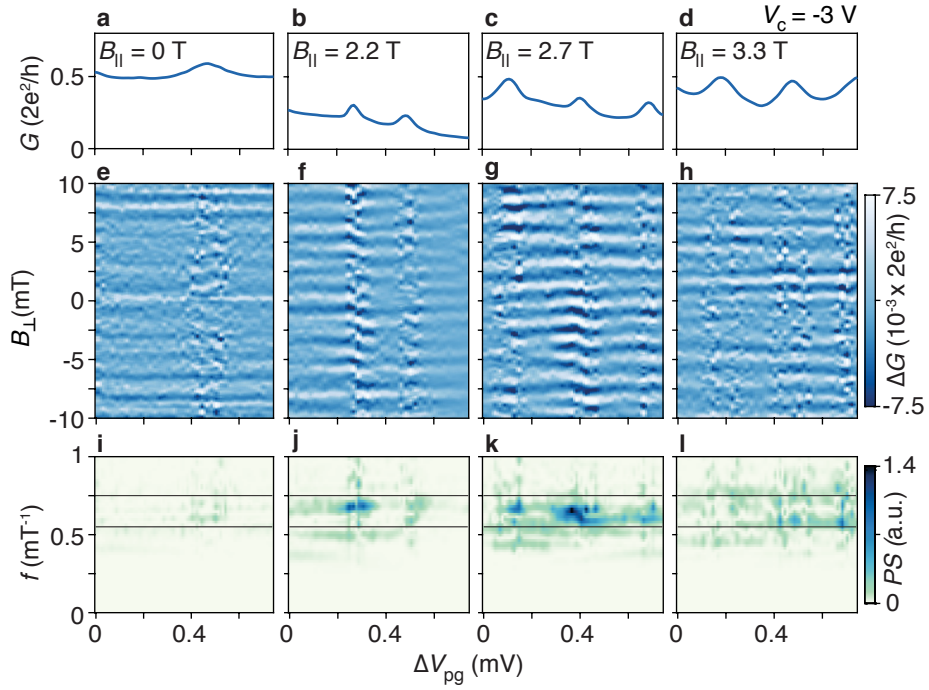


FIG. 2. **Evolution of conductance oscillations in parallel magnetic field.** Magnetoconductance for parallel field values  $B_{\parallel} = 0, 2.2, 2.7$ , and  $3.3$  T (left to right). **a-d**, Zero-bias differential conductance  $G(B_{\perp} = 0)$  versus gate voltage  $V_{\text{pg}}$  used to control electron occupation. **e-h**, Conductance  $\Delta G$  as a function of  $V_{\text{pg}}$  and perpendicular magnetic field  $B_{\perp}$  controlling the flux in the interferometer with corresponding power spectrums in **i-l** (solid black lines indicate the frequency window bounding the Aharonov-Bohm oscillations).  $\Delta G$  is the conductance with a subtracted slowly varying background.  $\Delta V_{\text{pg}} = 0$  corresponds to  $V_{\text{pg}} = -1.896$  V.

conducting Coulomb island [8, 9, 23, 25–28]. At high fields, the  $1e$  periodic diamonds show a discrete zero-bias state for consecutive charge degeneracy points that is well separated from the superconducting gap (Fig. 1e). This sub-gap feature remained at zero bias until the superconducting gap closure, and persists for 3 mV in  $V_{\text{pg}}$ , corresponding to an energy range of 0.8 meV. Below, we show that the ZBP was sensitive to rotations of the in-plane field. Overall, these observations are consistent with a MZM picture. The magnitude of  $B_{\parallel}$  where  $1e$  periodicity is observed is in agreement with ZBPs measured in tunneling spectroscopy in InAs 2DEGs [6]. In contrast, as a function of  $B_{\perp}$  the peak spacing remained even-odd, and discrete ZBPs on consecutive peaks were not observed in spectroscopy (see Supplementary Fig. S.2). The normal state of the Coulomb island appears above  $B_{\parallel} \sim 3$  T with  $E_c = 80$   $\mu$ eV (Fig. 1f).

The reference arm of the AB interferometer was connected by tuning  $V_c$  (see in Figs. 2a-d). Figures 2e-h show the conductance  $\Delta G$  through the full interferometer (with smooth background subtracted [29]) as a function of  $B_{\perp}$  and gate voltage  $V_{\text{pg}}$ , which controls the occupancy of the island. The power spectrum (PS) of  $\Delta G(B_{\perp})$  is shown in Fig. 2(i-l). Figure 2e shows small oscillations in  $\Delta G(B_{\perp})$  for the  $2e$  periodic peaks at  $B_{\parallel} = 0$  T. At  $B_{\parallel} = 2.2$  T, where the peak spacing was even-odd

(Fig. 2f), the conductance showed a moderate oscillation amplitude with a period  $\Delta B_{\perp} = 1.5$  mT, and a PS signal peaked around  $f = 0.65$  mT $^{-1}$ . The period  $\Delta B_{\perp}$  is consistent with a single flux quantum  $h/e$  piercing the interferometer, indicating coherent transport of single electrons. At higher parallel field,  $B_{\parallel} = 2.7$  T, the CB peak spacing was uniformly  $1e$ , and oscillation amplitude was maximal (see Figs. 2g,k). The oscillation amplitude was largest on the CB peaks and smaller in the valleys. When the Coulomb island was driven normal,  $B_{\parallel} > 3$  T, conductance oscillations were reduced, becoming comparable to oscillation amplitude seen at low parallel field (Fig. 2h,l).

It is interesting to compare the  $B_{\parallel}$  dependence of the AB oscillation amplitude to the corresponding field dependence of the lowest sub-gap state,  $E_0(B_{\parallel})$ , of the island. To quantify the oscillations amplitude,  $\langle \tilde{A} \rangle$ , we compute the integrated power spectrum over a band of frequencies marked by horizontal lines in Fig. 2, then average over Coulomb peaks and valleys. The sub-gap energy is found from the difference between even and odd CB peak spacings, averaged separately,  $\langle S \rangle = \langle S_e \rangle - \langle S_o \rangle$ . As seen in Fig. 3a,  $\langle S \rangle$  remains constant as a function of  $B_{\parallel}$  (indicating  $2e$  transport) until a sub-gap state moves below  $E_c$ , reaching zero at 2.2 T without overshoot (as expected for MZMs in a long wire). At low fields, where

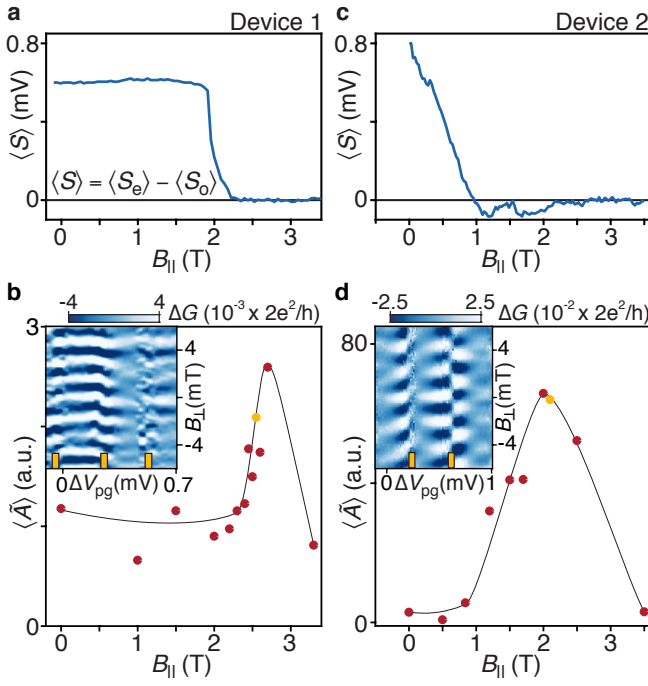


FIG. 3. Coulomb peak spacing difference and oscillation amplitude. **a,c**, Peak spacing difference  $\langle S \rangle$  as a function of parallel magnetic field  $B_{\parallel}$  for devices 1 and 2. **b,d**, Aharonov-Bohm oscillation amplitude  $\langle \tilde{A} \rangle$  as a function of  $B_{\parallel}$ . The solid line is a guide to the eye. Insets show characteristic magnetoconductance  $\Delta G$  as a function of gate voltage  $V_{pg}$  controlling electron occupancy and perpendicular magnetic field  $B_{\perp}$  controlling the magnetic flux in the interferometer in the 1e regime (indicated by yellow markers in the main panel). Yellow ticks show CB peak positions.  $\Delta V_{pg} = 0$  corresponds to  $V_{pg} = -1.896$  V and -0.945 V for **b** and **d**, respectively.

the CB periodicity was  $2e$ , the oscillation amplitude  $\langle \tilde{A} \rangle$  is small (Fig. 3b). When  $\langle S \rangle$  approaches zero at high fields ( $B_{\parallel} > 2$  T),  $\langle \tilde{A} \rangle$  exhibits a sharp increase that coincides with the  $2e$  to 1e transition. Above 3 T, the Coulomb island was in the normal state and  $\langle \tilde{A} \rangle$  returned to the low value found in the low-field 2e regime.

Figure 3c,d shows a similar study for device 2. In Fig. 3c,  $\langle S \rangle$  shows strong even-odd below 1 T, fluctuates around  $\langle S \rangle = 0$  between 1-2 T, then settles to 1e ( $\langle S \rangle = 0$ ) above 2 T. CB spectroscopy reveals a discrete state that oscillates around zero energy in both  $B_{\parallel}$  and  $V_{pg}$  without forming a robust zero-bias peak (see Supplementary Fig. S.4). This behaviour is compatible with hybridized MZMs or extended Andreev bound states (ABS) [9]. Figure 3d shows that phase coherent transport first appears above 1 T and  $\langle \tilde{A} \rangle$  gradually increases until reaching a maximum amplitude for 1e peak spacing at 2.1 T, before diminishing in the normal state.

Upon changing the charge occupancy by one electron we found a transmission phase shift of  $\pi$  occurs in the 1e regime (see insets of Fig. 3). For device 2, we observed

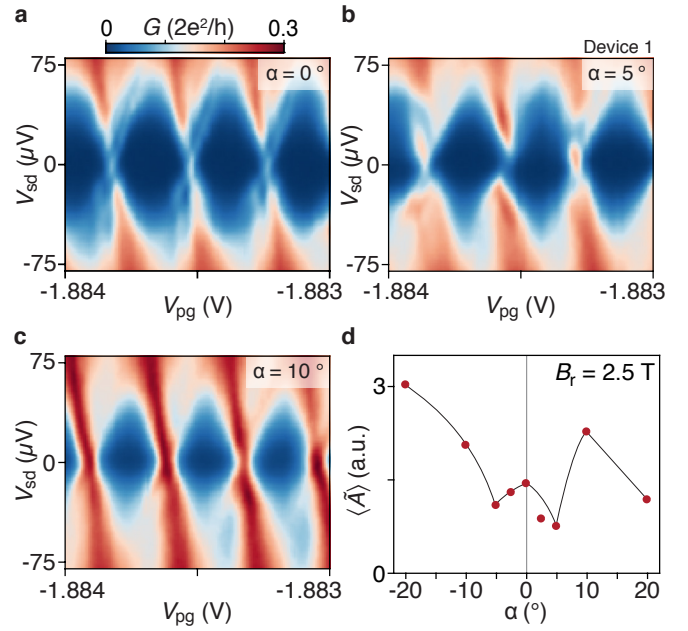


FIG. 4. In-plane magnetic field rotations. **a-c**, Differential conductance  $G$  as a function of gate voltage  $V_{pg}$  controlling electron occupancy and source-drain bias voltage  $V_{sd}$  showing Coulomb diamonds for in-plane rotation angles of  $\alpha = 0$  (a),  $5^\circ$  (b), and  $10^\circ$  (c) with  $\alpha = 0$  corresponding to  $B_{\parallel} = 2.5$  T. **d**, Oscillation amplitude  $\langle \tilde{A} \rangle$  as a function of in-plane rotation angle  $\alpha$  for  $B_r = 2.5$  T. The solid line is a guide to the eye.

phase lapses in the CB valley leading to the same side of CB peaks having the same phase, while device 1 showed a more rigid phase in the valleys (also see Supplementary Fig. S.5) [19–21]. The pattern of phase lapses, and the difference between devices, is currently not understood and appears to vary depending on gate voltage configurations.

We next investigate the angular dependence of the in-plane magnetic field for device 1. Figure 4a shows 1e Coulomb diamonds at  $B_{\parallel} = 2.5$  T with a discrete state at each charge degeneracy point (see Fig. 1e). Rotating the magnetic field by an angle  $\alpha = 5^\circ$  (keeping the in-plane field magnitude  $B_r = 2.5$  T constant) lifted the discrete state from zero energy and transitioned the peak spacing to even-odd, whereas at  $\alpha = 10^\circ$  the periodicity was again 1e but without a discrete ZBP. Small rotations ( $|\alpha| < 7.5^\circ$ ) reduced the oscillation amplitude, as expected for even-odd periodicity. However, at larger angles ( $|\alpha| > 10^\circ$ ) where the discrete zero-bias peak was absent, a strong interference signal was observed (Fig. 4d). An in-plane field-angle sensitivity of the zero-energy mode is consistent with a MZM interpretation. However, the observation of coherent transport in the absence of a discrete zero-energy mode suggests trivial quasiparticles are phase coherent over the length of the island.

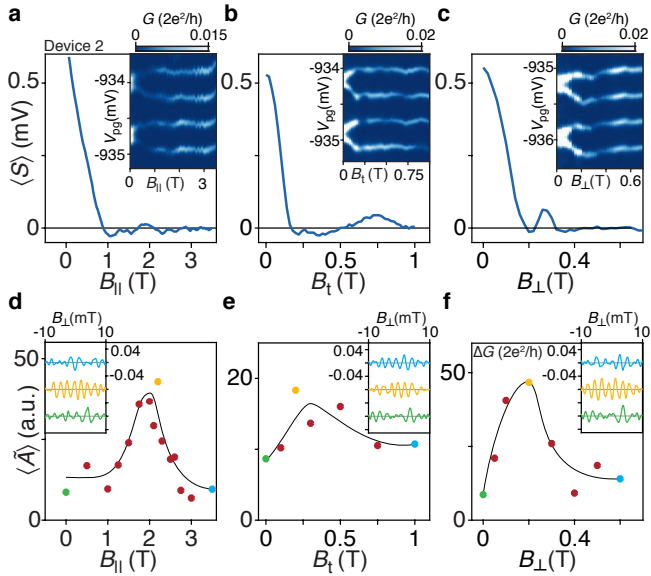


FIG. 5. **Orthogonal magnetic fields.** **a-c**, Peak spacing difference  $\langle S \rangle$  as a function of magnetic fields  $B_{\parallel}$ ,  $B_t$ , and  $B_{\perp}$  for **a**, **b**, and **c**, respectively. Insets show the zero-bias differential conductance  $G$  as a function of magnetic field and gate voltage  $V_{pg}$  controlling electron occupancy with the reference arm closed. **d-f**, Oscillation amplitude  $\langle \tilde{A} \rangle$  as a function of magnetic fields  $B_{\parallel}$ ,  $B_t$ , and  $B_{\perp}$  for **d**, **e**, and **f**, respectively. The solid lines are a guide to the eye. Insets show magnetoconductance  $\Delta G$  traces as a function of small perpendicular magnetic field  $B_{\perp}$ . Curves with the largest AB oscillation amplitude are shown for specific magnetic fields indicated by the marker color in the main panel.

To further explore the dependence on in-plane field, we study the effect of magnetic fields aligned orthogonal to the wire axis ( $B_{\perp}$  and  $B_t$ ) on the oscillation amplitude in device 2. In Fig. 5a-c, the peak spacing difference  $\langle S \rangle$  is shown as a function of the three field directions. For the two orthogonal fields,  $\langle S \rangle$  reaches zero at  $\sim 0.2$  T, in comparison to 1 T for  $B_{\parallel}$ . A perpendicular field  $B_{\perp}$  induces large oscillations in  $\langle S \rangle$  before the normal state transition at 0.4 T (Fig. 5c) and a transverse field  $B_t$  causes  $\langle S \rangle$  to oscillate around zero (Fig. 5b). Figures 5d-f shows the oscillations amplitude  $\langle \tilde{A} \rangle$  for the three field directions. In all directions, coherent transport was observed, with oscillation amplitude first increasing as  $\langle S \rangle$  approached zero. This indicates that the oscillation amplitude is dictated by the energy  $E_0$  in all field directions and shows that interference is not unique to a parallel magnetic field.

Finally, we comment on the physical mechanism that correlates the oscillation amplitude to the energy of  $E_0$ . At low fields, the Coulomb island favours an even parity where transport of electrons occurs as two sequential tunnelling events on either end of the Coulomb island [23, 26]. The two electrons acquire the condensate phase when forming a Cooper pair, which suppresses

single-electron coherence. At moderate fields, a discrete sub-gap state is brought below  $E_c$  and a single-electron transport channel is opened, allowing for coherent resonant tunnelling through the Coulomb island. Finally, when the Coulomb island is in the normal state, we interpret the reduction in interference signal to reflect the short coherence length in the diffusive Al wire.

In conclusion, the observation of AB interference combined with a stable discrete zero-energy states is consistent with current MZM predictions and allows for the contribution of ABS localized at the ends of the wire to be excluded [15], which have been a possible interpretation of the previously observed ZBPs in local tunneling experiments [11]. Our results also highlight the contribution to coherent transport by electronic modes extending over the full length of the island (at least in the length investigated here) and demonstrates how AB interference alone is not sufficient evidence to draw conclusions about electron teleportation via MZMs. To discriminate between trivial and topological states, stable  $1e$  peak spacing and discrete zero-bias conductance peaks at successive charge degeneracy points must accompany AB interference. Another approach could involve the suppression of trivial extended modes by increasing the wire length to greatly exceed the diffusive coherence length  $\xi = \sqrt{\xi_0 l_e} \sim 1 \mu\text{m}$  (for  $\Delta = 75 \mu\text{eV}$  at  $B_{\parallel} = 2.5$  T), where  $\xi_0$  is the clean coherence length and  $l_e \sim 300 \text{ nm}$  is the semiconducting mean free path [30].

These results suggest that InAs-Al 2DEGs are a promising route towards more complex experiments related to the braiding or fusion of MZMs. We have established Coulomb islands as coherent links necessary for topological qubit networks, as well as demonstrated that the transmission phase can measure the parity of the island. Future devices will take advantage of improved material quality to allow for increased wire lengths to suppress coherent trivial quasiparticle transport, allowing MZM contributions to be better separated from other potential contributions.

\* These authors contributed equally to this work.

<sup>†</sup> email: marcus@nbi.ku.dk

<sup>‡</sup> email: fni@ibm.zurich.com; Present address: IBM Research - Zurich, Sumerstrasse 4, 8803 Rschlikon, Switzerland.

- [1] Nayak, C., Simon, S. H., Stern, A., Freedman, M. & Sarma, S. D. Non-abelian anyons and topological quantum computation. *Rev. Mod. Phys.* **80**, 1083 (2008).
- [2] Karzig, T. *et al.* Scalable designs for quasiparticle-poisoning-protected topological quantum computation with Majorana zero modes. *Phys. Rev. B* **95**, 235305 (2017).
- [3] Fu, L. Electron Teleportation via Majorana bound states in a Mesoscopic Superconductor. *Phys. Rev. Lett.* **104**, 056402 (2010).

[4] Mourik, V. *et al.* Signatures of Majorana fermions in hybrid superconductor-semiconductor nanowire devices. *Science* **336**, 1003–1007 (2012).

[5] Deng, M. *et al.* Majorana bound state in a coupled quantum-dot hybrid-nanowire system. *Science* **354**, 1557–1562 (2016).

[6] Nichele, F. *et al.* Scaling of Majorana zero-bias conductance peaks. *Phys. Rev. Lett.* **119**, 136803 (2017).

[7] Zhang, H. *et al.* Quantized Majorana conductance. *Nature* **556**, 74–79 (2018).

[8] Albrecht, S. M. *et al.* Exponential protection of zero modes in Majorana islands. *Nature* **531**, 206–209 (2016).

[9] O’Farrell, E. C. T. *et al.* Hybridization of sub-gap states in one-dimensional superconductor/semiconductor Coulomb islands. *Phys. Rev. Lett.* **121**, 256803 (2018).

[10] Chiu, C.-K., Sau, J. D. & Sarma, S. D. Conductance of a superconducting Coulomb-blockaded Majorana nanowire. *Phys. Rev. B* **96**, 054504 (2017).

[11] Moore, C., Stanesu, T. D. & Tewari, S. Two-terminal charge tunneling: Disentangling Majorana zero modes from partially separated Andreev bound states in semiconductor-superconductor heterostructures. *Phys. Rev. B* **97**, 165302 (2018).

[12] Deng, M.-T. *et al.* Nonlocality of Majorana modes in hybrid nanowires. *Phys. Rev. B* **98**, 085125 (2018).

[13] Sau, J. D., Swingle, B. & Tewari, S. Proposal to probe quantum nonlocality of Majorana fermions in tunneling experiments. *Phys. Rev. B* **92**, 020511 (2015).

[14] Vijay, S. & Fu, L. Teleportation-based quantum information processing with Majorana zero modes. *Phys. Rev. B* **94**, 235446 (2016).

[15] Hell, M., Flensberg, K. & Leijnse, M. Distinguishing Majorana bound states from localized Andreev bound states by interferometry. *Phys. Rev. B* **97**, 161401 (2018).

[16] Drukier, C., Zirnstein, H.-G., Rosenow, B., Stern, A. & Oreg, Y. Evolution of the transmission phase through a Coulomb-blockaded Majorana wire. *Phys. Rev. B* **98**, 161401 (2018).

[17] Aharonov, Y. & Bohm, D. Significance of electromagnetic potentials in the quantum theory. *Phys. Rev.* **115**, 485 (1959).

[18] Yacoby, A., Schuster, R. & Heiblum, M. Phase rigidity and  $h/2e$  oscillations in a single-ring Aharonov-Bohm experiment. *Phys. Rev. B* **53**, 9583 (1996).

[19] Schuster, R. *et al.* Phase measurement in a quantum dot via a double-slit interference experiment. *Nature* **385**, 417–420 (1997).

[20] Avinun-Kalish, M., Heiblum, M., Zarchin, O., Mahalu, D. & Umansky, V. Crossover from ‘mesoscopic’ to ‘universal’ phase for electron transmission in quantum dots. *Nature* **436**, 529–533 (2005).

[21] Edlbauer, H. *et al.* Non-universal transmission phase behaviour of a large quantum dot. *Nat. Commun.* **8**, 1710 (2017).

[22] Shabani, J. *et al.* Two-dimensional epitaxial superconductor-semiconductor heterostructures: A platform for topological superconducting networks. *Phys. Rev. B* **93**, 155402 (2016).

[23] Hekking, F. W. J., Glazman, L. I., Matveev, K. A. & Shekhter, R. I. Coulomb blockade of two-electron tunneling. *Phys. Rev. Lett.* **70**, 4138 (1993).

[24] Van Heck, B., Lutchyn, R. M. & Glazman, L. I. Conductance of a proximitized nanowire in the Coulomb blockade regime. *Phys. Rev. B* **93**, 235431 (2016).

[25] Tuominen, M. T., Hergenrother, J. M., Tighe, T. S. & Tinkham, M. Experimental evidence for parity-based  $2e$  periodicity in a superconducting single-electron tunneling transistor. *Phys. Rev. Lett.* **69**, 1997 (1992).

[26] Eiles, T. M., Martinis, J. M. & Devoret, M. H. Even-odd asymmetry of a superconductor revealed by the Coulomb blockade of Andreev reflection. *Phys. Rev. Lett.* **70**, 1862 (1993).

[27] Higginbotham, A. P. *et al.* Parity lifetime of bound states in a proximitized semiconductor nanowire. *Nat. Phys.* **11**, 1017–1021 (2015).

[28] Shen, J. *et al.* Parity transitions in the superconducting ground state of hybrid InSb-Al Coulomb islands. *Nat. Commun.* **9**, 4801 (2018).

[29] Savitzky, A. & Golay, M. J. Smoothing and differentiation of data by simplified least squares procedures. *Anal. Chem.* **36**, 1627–1639 (1964).

[30] Tinkham, M. *Introduction to superconductivity* (Courier Corporation, 2004).

[31] Ludwig, T. & Mirlin, A. D. Interaction-induced dephasing of Aharonov-Bohm oscillations. *Phys. Rev. B* **69**, 193306 (2004).

**Acknowledgments** This work was supported by Microsoft Corporation, the Danish National Research Foundation, and the Villum Foundation. We thank Karsten Flensberg, Joshua Folk, Michael Hell, Andrew Higginbotham, Torsten Karzig, Panagiotis Kotetes, Martin Leijnse, Tommy Li, Alice Mahoney, and Ady Stern for useful discussions.

## METHODS

The devices were fabricated on wafers grown by molecular beam epitaxy on a InP substrate. The wafer stack consists of a  $1\ \mu\text{m}$  graded  $\text{In}_{1-x}\text{Al}_x\text{As}$  insulating buffer, a  $4\ \text{nm}$   $\text{In}_{0.81}\text{Ga}_{0.19}\text{As}$  bottom barrier, a  $5\ \text{nm}$  InAs quantum well, and a top barrier consisting of  $5\ \text{nm}$   $\text{In}_{0.9}\text{Al}_{0.1}\text{As}$  for device 1 and  $10\ \text{nm}$   $\text{In}_{0.81}\text{Ga}_{0.19}\text{As}$  for device 2. A  $7\ \text{nm}$  film of epitaxial Al was then grown in-situ without breaking the vacuum of the chamber. The InAs 2DEGs were characterized with a Hall bar geometry (Al removed), which showed a peak mobility of  $\mu = 17,000\ \text{cm}^2\text{V}^{-1}\text{s}^{-1}$  for an electron density of  $n = 1.7 \times 10^{12}\ \text{cm}^{-2}$  and  $n = 7.5 \times 10^{11}\ \text{cm}^{-2}$  for device 1 and device 2, respectively.

Devices were fabricated using standard electron beam lithography techniques. The devices were electrically isolated by etching mesa structures by first removing the top Al film with Al etchant Transene D, followed by a deep III-V chemical wet etch  $\text{H}_2\text{O} : \text{C}_6\text{H}_8\text{O}_7 : \text{H}_3\text{PO}_4 : \text{H}_2\text{O}_2$  (220:55:3:3). Next, the Al film on the mesa was selectively etched with Al etchant Transene D to produce the Al strip. A  $25\ \text{nm}$  thick layer of insulating  $\text{HfO}_2$  was grown by atomic layer deposition at a temperature of  $90^\circ\text{C}$  over the entire sample. Top gates of Ti/Au ( $5/25\ \text{nm}$ ) were then evaporated and connected to bonding pads with leads of Ti/Au ( $5/250\ \text{nm}$ ).

Electrical measurements were performed by standard lock-in techniques at 166 Hz by applying the sum of a variable dc bias voltage  $V_{sd}$  and an ac excitation voltage of 3 to 10  $\mu$ V applied to one of the top ohmic contacts as shown in Fig. 1a. The resulting current across the device was recorded by grounding a bottom ohmic via a low-impedance current-to-voltage converter, and the four terminal voltage was measured by an ac voltage amplifier with an input impedance of 500 M $\Omega$ . All measurements were taken in a dilution refrigerator with a base temperature of 20 mK and an electron temperature of 40 mK estimated by the temperature dependence saturation of ZBP conductance [6].

## SUPPLEMENTARY INFORMATION

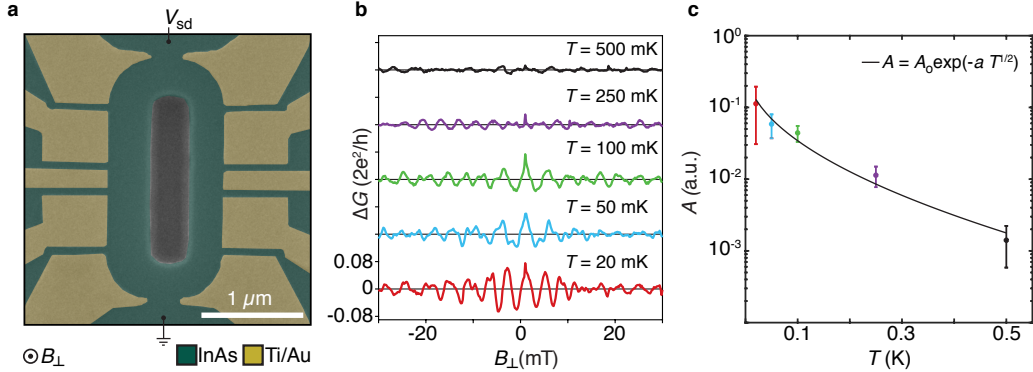
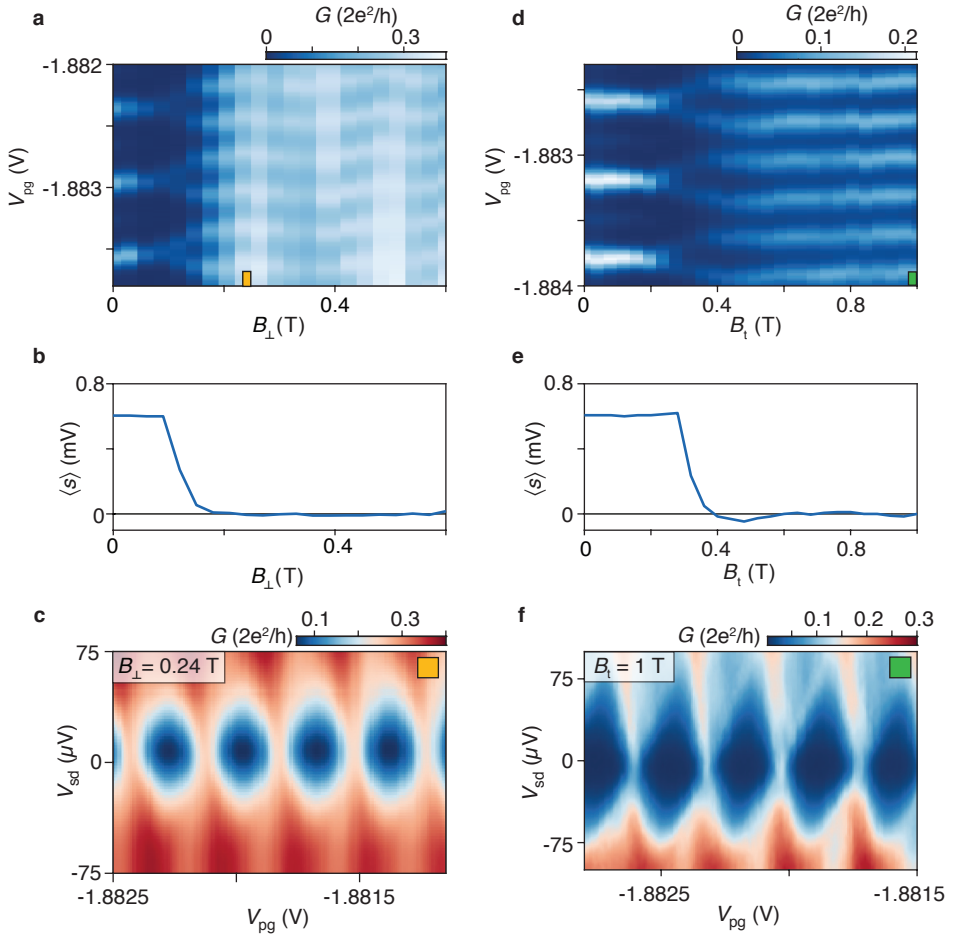
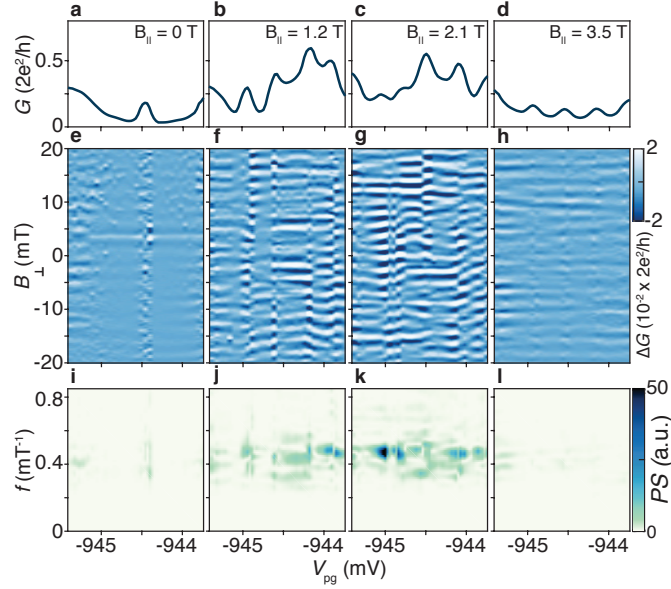


FIG. S.1. **Temperature dependence of Aharonov-Bohm oscillations in a normal 2DEG.** **a**, False-colour electron micrograph of a normal conducting AB interferometer defined in an InAs 2DEG (green) by gates (Ti/Au). The hole forming the interferometer center is created by a wet etch. **b**, Magnetocconductance  $\Delta G$  as a function of perpendicular magnetic field  $B_{\perp}$  controlling the flux in the interferometer for several temperatures. Periodic oscillations are observed with a frequency of  $f \sim 0.26 \text{ mT}^{-1}$ , which agrees with a single magnetic flux quantum  $h/e$  piercing the interferometer loop. **c**, Temperature dependence of the AB oscillations amplitude  $A$  measured from the power spectrum of the curves in **b**. For a diffusive interferometer, the amplitude  $A = A_0 \exp(-L/l_{\phi}(T))$  where  $l_{\phi}(T) \propto T^{-1/2}$  is the phase coherence length and  $L = 4.5 \mu\text{m}$  is the circumference of the interferometer [31]. The exponential fit  $A = A_0 \exp(-a T^{1/2})$  gives a base temperature coherence length of  $l_{\phi}(20 \text{ mK}) = 4 \mu\text{m} \pm 1 \mu\text{m}$ . Error bars show the standard deviation between 4 data sets at each temperature.



**FIG. S.2. Transverse and perpendicular fields for device 1 in the regime of Fig. 1.** **a**, Zero-bias differential conductance  $G$  as a function of gate voltage  $V_{pg}$  controlling electron occupancy and perpendicular field,  $B_{\perp}$ . **b**, Coulomb peak spacing difference  $\langle S \rangle$  as a function of  $B_{\perp}$ . **c**, Differential conductance  $G$  as a function of source-drain bias voltage  $V_{sd}$  and  $V_{pg}$  showing Coulomb diamonds for  $B_{\perp} = 0.24$  T. **d**, Zero-bias differential conductance  $G$  as a function of  $V_{pg}$  and transverse field,  $B_t$ . **e**, Coulomb peak spacing difference  $\langle S \rangle$  as a function of  $B_t$ . **f**, Differential conductance  $G$  as a function of  $V_{sd}$  and  $V_{pg}$  showing Coulomb diamonds for  $B_t = 1$  T. The field directions are represented in Fig. 1a.



**FIG. S.3. Conductance oscillations evolutions in parallel field for Device 2.** Magnetoconductance for parallel field values  $B_{\parallel} = 0, 1.2, 2.1$ , and  $3.5$  T (left to right). **a-d**, Zero-bias differential conductance  $G(B_{\perp} = 0)$  versus gate voltage  $V_{\text{pg}}$  controlling electron occupation. **e-h**, Magnetoconductance  $\Delta G$  as a function of  $V_{\text{pg}}$  and perpendicular field  $B_{\perp}$  controlling the flux in the interferometer with corresponding power spectra in **i-l**. A single flux quantum piercing the loop area  $A_{\text{loop}} \sim 1.8 \mu\text{m}^2$  corresponds to a frequency  $f_{\text{loop}} = A_{\text{loop}}/(h/e) \sim 0.44 \text{ mT}^{-1}$ . **e-l**, a slowly varying background has been subtracted.

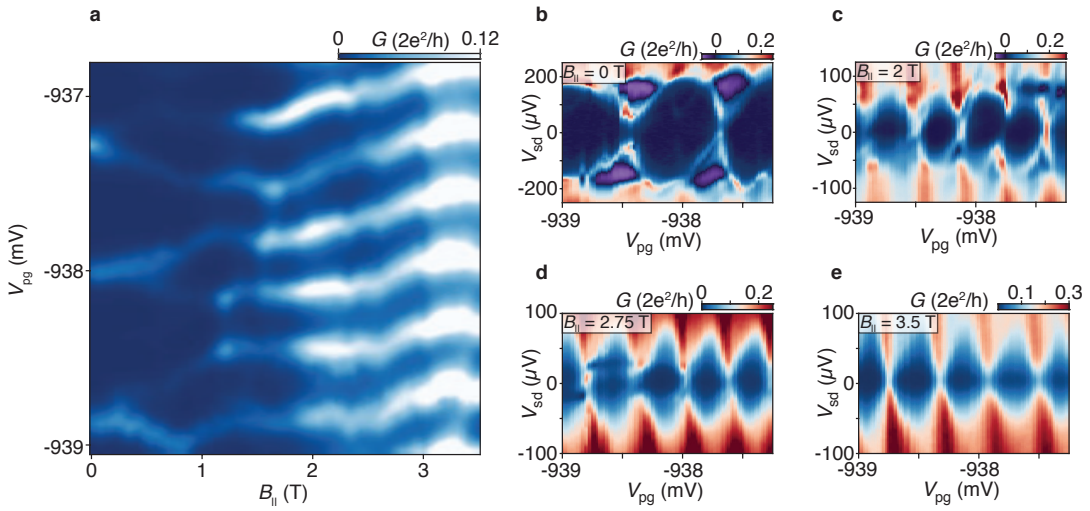


**FIG. S.4. Coulomb blockade for device 2.** **a**, Zero-bias differential conductance  $G$  as a function of parallel magnetic field  $B_{\parallel}$  and gate voltage  $V_{\text{pg}}$  controlling the electron occupancy with the reference arm closed. **b-e**, Differential conductance  $G$  as a function of voltage bias  $V_{\text{sd}}$  and  $V_{\text{pg}}$  for  $B_{\parallel} = 0$  T (**b**), 2 T (**c**), 2.75 T (**d**), and 3.5 T (**e**).

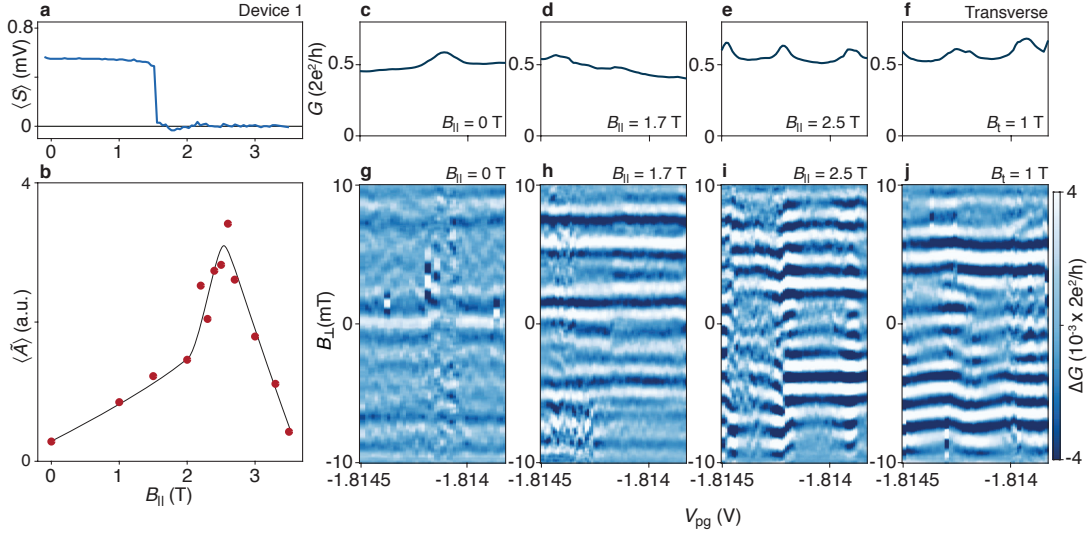


**FIG. S.5. Second gate configuration of device 1.** **a**, Peak spacing difference  $\langle S \rangle$  as a function of parallel magnetic field  $B_{\parallel}$ . **b**, Aharonov-Bohm oscillation amplitude  $\langle \tilde{A} \rangle$  as a function of  $B_{\parallel}$ . The solid line is a guide to the eye. **c-j**, Magnetoconductance for parallel magnetic fields  $B_{\parallel} = 0$  T, 1.7 T, and 2.5 T and transverse magnetic field  $B_t = 1$  T (left to right). **c-f**, Zero-bias differential conductance  $G(B_{\perp} = 0)$  versus gate voltage  $V_{pg}$  used to control electron occupation. **g-j**, Magnetoconductance  $\Delta G$  as a function of  $V_{pg}$  and perpendicular magnetic field  $B_{\perp}$  controlling the flux in the interferometer.